Petroleum Science 23 (2026) 5450–5461

Contents lists available at ScienceDirect

Petroleum Science

journal homepage: www.keaipublishing.com/en/journals/petroleum-science

Original Paper

Improved AVA imaging for vector-based elastic reverse time migration using angle-domain dot-product imaging condition

Shu-Kui Zhang [a,b], Shao-Ping Lu [c,d,*], Zhi-Jing Liu [a,b], Han Wu [e,f], Gang Fang [a,b]

[a] State Key Laboratory for Tunnel Engineering, Jinan, 250061, Shandong, China
[b] School of Future Technology, Shandong University, Jinan, 250002, Shandong, China
[c] School of Earth Sciences and Engineering, Sun Yat-Sen University, Zhuhai, 519000, Guangdong, China
[d] Southern Marine Science and Engineering Guangdong Laboratory (Zhuhai), Zhuhai, 519000, Guangdong, China
[e] Exploration and Development Research Department, CNOOC Research Institute Ltd., Beijing, 100028, China
[f] National Engineering Research Center of Offshore Oil and Gas Exploration, Beijing, 100028, China

ARTICLE INFO

Article history:
Received 4 September 2025
Received in revised form
10 January 2026
Accepted 15 April 2026
Available online 21 April 2026

Edited by Meng-Jiao Zhou

Keywords:
Angle domain common image gathers
Vector-based ERTM
AVA
Imaging conditions

ABSTRACT

This paper proposes modified angle-domain dot-product imaging conditions for vector-based elastic reverse time migration, which yields PP and PS angle gathers that capture improved amplitude-versus-angle (AVA) information. The vector P-wavefields and converted S-wavefields can be constructed by separating the coupled elastic wavefields. A simple and stable dot-product imaging condition can be employed to generate scalar PP and PS angle gathers. However, estimating amplitudes via migrated angle gathers using the conventional angle-domain dot-product imaging conditions leads to inaccurate AVA information. The inaccuracy arises because the dot-product imaging condition does not correctly represent seismic PP and PS reflectivity. Hence, the relationship between the dot-product imaging conditions and the reflection coefficients is explicitly derived in this paper. Then, the modified angle-domain dot-product imaging conditions for calculating PP and PS angle gathers are presented based on the kinematic characteristics of the vector P- and S-wavefields, along with an explanation of their amplitude correction mechanism. Finally, simple layer models with positive and negative reflection polarities are used to compute angle gathers to demonstrate the accuracy of the proposed imaging conditions in calculating AVA imaging. Numerical results from the Marmousi2 model validate the effectiveness and correctness of the proposed imaging conditions in complex media.

1. Introduction

Prestack elastic wave reverse time migration (ERTM) (Chang and McMechan, 1987, 1994) is a technique used multicomponent seismic data to obtain subsurface structural information. To avoid crosstalk artifacts arising from different propagating wave modes, a crucial step in ERTM is to separate P- and S-waves (Yan and Sava, 2008) instead of imaging using unseparated elastic wavefields directly. Based on different wavefield separation strategies, two ERTM implementation algorithms have been proposed (Sun and McMechan, 2001; Wang and McMechan, 2015).

One approach relies on the elastic-wave equation to construct elastic wavefields (Sun, 1999), where scalar P-waves and vector S-waves are obtained by applying the divergence and curl operators (Aki and Richards, 2002) to the elastic wavefields. To provide amplitude-preserving imaging results, the amplitude correction caused by the spatial derivatives (Sun et al., 2011; Nguyen and McMechan, 2015) needs to be implemented. Additionally, the converted-wave images calculated using the elastic-wave equation suffer from the polarity reversal problem (Balch and Erdemir, 1994). To address the above issue, Du et al. (2012) used the Poynting vectors to determine the polarity of the converted wavefield, while Gong et al. (2016) chose to utilize the optical flow vector. Duan and Sava (2015) proposed new scalar imaging conditions based on the isotropic elastic wave equation. Using the geometric relationships between the wavefields, propagation directions, and the reflector orientation and polarization directions, the proposed imaging conditions can generate a single scalar

* Corresponding author.
E-mail address: lushaoping@mail.sysu.edu.cn (S.-P. Lu).
Peer review under the responsibility of China University of Petroleum (Beijing).

https://doi.org/10.1016/j.petsci.2026.04.023
1995-8226/

image characterizing the PS reflectivity without being affected by polarity reversal. To summarize, P- and S-waves in the above wavefield separation approach do not directly participate in wavefield extrapolation.

Another P- and S-wave wavefield separation approach considers the elastic wavefields as decoupled vector P- and S-waves (Ma and Zhu, 2003; Zhang et al., 2007) and incorporates them into the wavefield extrapolation. This wavefield separation method relies on the vector-based elastic wave equation, producing P- and S-waves with preserved amplitude and phase information (Wang and McMechan, 2015). To estimate scalar imaging results reflecting reflection coefficients, it is necessary to develop suitable imaging conditions using vector wavefields. According to the definition of reflection coefficients, Wang and McMechan (2015) presented a vector-based imaging condition using an excitation-amplitude algorithm. This imaging condition can provide accurate PP and PS reflection coefficients without amplitude and phase correction. Another imaging condition directly applies the dot-product operator to the vector wavefields, often named the scalar imaging condition. This imaging condition involves the application of vector wavefields to the conventional cross-correlation imaging condition (Claerbout, 1971); thus, it is stable and can provide physically meaningful subsurface imaging. Wang et al. (2016) extended the cross-correlation imaging condition with the imaging amplitude balance for vector wavefields in transversely isotropic media. Using the scalar P-wave derived from the P-wave stress, Zhou et al. (2019) gave a scalar PP imaging condition to generate amplitude-preserving PP imaging results. For PS images, they use the wavefield energy and the signs of PS images to generate amplitude-preserving PS imaging results. Based on the inverse-scattering imaging condition, Yang et al. (2021) developed the elastic imaging condition for vector wavefields to avoid the polarity reversal in P- and S-waves at the opening angles and the Brewster angles, respectively.

Although the dot-product imaging condition has been widely applied in vector-based ERTM, the imaging amplitude is affected by an angle-dependent factor from the dot-product operator. For PP imaging, its amplitude contains a weight operator from the cosine of the opening angle between the source and receiver wavefields. The amplitude sign changes, especially when the opening angle is greater than 90°, and unwanted polarity reversal issues occur at a certain offset. Due to the differences in the vibration direction of S-waves, PS-image amplitude still contains a weight operator from the sine, though not the cosine, of the opening angle. To address the sign change issue in PP imaging, Du et al. (2017) proposed solutions by muting imaging amplitudes at large opening angles. Zhang et al. (2018) introduced the Laplace operator into the dot-product imaging condition and incorporated an additional weight operator to resolve the polarity reversal issue and attenuate low wavenumber noises (Zhang and Sun, 2009; Liu et al., 2011). Instead of using the dot-product imaging condition, Yang et al. (2021) used the inverse-scattering imaging condition (Whitmore and Crawley, 2012) for the vector elastic wavefields, obtaining PP and PS imaging results unaffected by polarity reversal issues.

After obtaining imaging results, geological structural interpretations can be performed. As extension imaging, common image gathers (CIGs) are valuable for implementing quantitative seismic interpretation (Wang et al., 2005), such as lithological identification, fluid detection, and discerning hydrocarbon reservoirs. Angle-domain CIGs (ADCIGs or angle gathers) bin imaging amplitudes of each imaging point according to imaging angles, directly yielding AVA analysis. Two primary algorithms are utilized to compute angle gathers based on conventional CIG generation strategies. One approach initially calculates subsurface offset to generate subsurface offset CIGs and then are converted to angle gathers (Sava and Fomel, 2003, 2006). By establishing the respective relationships between the incident and reflection angles with the subsurface offset, Rosales and Biondi (2005) and Rosales et al. (2008) extended the subsurface offset-to-angle algorithm to ERTM. Employing a consistent computational approach, Yan and Sava (2010) and Zhao et al. (2020) successfully built a velocity model for both P- and S-waves using elastic-wave angle gathers converted from subsurface offset gathers.

An alternative approach entails the direct wavefield propagation angle calculation for extracting angle gathers (Yoon and Marfurt, 2006; Xu et al., 2011), where the Poynting vector method has been demonstrated as effective and accurate for angle calculation. This method remains applicable for computing elastic wave angle gathers. Using source Poynting vectors and the normal direction calculated from instantaneous frequency, Zhang and McMechan (2011) computed incident-angle-based elastic wave angle gathers by applying the cross correlation imaging condition. Wang and McMechan (2015) determined the opening angle using source and receiver Poynting vectors, subsequently obtaining elastic wave angle gathers based on the vector-based imaging condition. Using incident propagation vector and reflector normal directions calculated instantaneous wavenumber direction, Khaksar and McMechan (2020) developed an efficient method to generate 3D angle- and azimuth-domain CIGs. Recently, many accurate and stable methods have been proposed to calculate Poynting vectors and applied to get high-quality elastic wave angle gathers (Tang and McMechan, 2018; Yang et al., 2022).

This paper aims to obtain elastic wave angle gathers mirroring improved AVA information using vector-based ERTM. We extend the dot-product imaging condition into the angle domain and derive the relationship between reflection coefficients and imaging amplitudes. We introduce corrective operators to get new angle-domain dot-product imaging conditions to eliminate the impact of the angle-dependent factors and the signs of the reflection polarities. Then, we analyze wavefield propagation characteristics for positive and negative reflection coefficients separately due to the differences in P- and S-wave vibration directions. Based on the above kinematic analysis of elastic waves, we derive a stable and easy-to-implement imaging condition named the corrected angle-domain dot-product imaging condition. Using simple and complex models, we validate the accuracy and robustness of the proposed imaging conditions in calculating improved AVA information.

The paper will be organized as follows. Firstly, we introduce the angle-domain dot-product imaging conditions for vector-based ERTM and derive their relationship between reflection coefficients. Then, we give the corrected angle-domain dot-product imaging conditions based on the kinematic analysis of P- and S-waves. A simple model is used to validate the accuracy of the proposed imaging conditions. Finally, we use a complex model to validate the correctness of the imaging conditions in calculating AVA information.

2. Methodology

The computation of elastic wave angle gathers primarily comprises two main parts: computing imaging amplitudes based on ERTM, and binning the amplitudes based on the computed imaging angles. There are two strategies to calculate vector P- and S-wave wavefields for implementing vector-based ERTM, including calculating P- and S-wave wavefields simultaneously (Ma and Zhu, 2003; Li et al., 2007) or introducing the auxiliary P-wave stresses to calculate P-wave first (Xiao and Leaney, 2010). Wang and McMechan (2015) demonstrated that the above two strategies are equivalent. This paper uses the second strategy to calculate vector P- and S-wave wavefields.

For calculating wavefield propagation direction, many methods have been proposed and widely used in practice. In this paper, we use the source Poynting vectors and dipping angles presented by Yoon et al. (2011). This method calculates only one imaging angle at each imaging point from one shot gather by searching for the Poynting vectors with major contributions, named the one-shot, one-position, and one-angle binning strategy (Yoon et al., 2011; Zhang and Lu, 2022). Firstly, this method calculates the Poynting vectors using the source wavefields and then obtains the incidence angles utilizing the calculated Poynting vectors and the dipping angles. Compared to the receiver wavefields constructed using the seismic data, the source wavefields have less overlap and can avoid noises in the receiver wavefields caused by the seismic data. Secondly, this method chooses a time window to pick the amplitude of the Poynting vectors at each imaging location. This strategy aims to address the instability problem that arises due to the amplitude zero point of the Poynting vector. Therefore, this method can calculate imaging angles accurately and is easy to implement. We extend this method to calculate imaging angles for vector-based ERTM. This paper aims to elucidate the relationship between the imaging condition and reflection coefficients. Therefore, we primarily discuss the impact of imaging conditions used for computation on AVA imaging.

The following section briefly overviews the dot-product imaging condition and derives its relationship with reflection coefficients.

2.1. The relation between reflection coefficients and the angle-domain dot-product imaging conditions

In this subsection, we first show the decoupled P- and S-wave propagation equation used to calculate the vector P- and S-wavefields. Based on the expression of the cross-correlation imaging condition, the angle-domain dot-product imaging conditions for calculating scalar imaging results using vector wavefields are given. Subsequently, the relationship between the dot product imaging condition and the reflection coefficient is derived using the definition of the reflection coefficient.

A displacement vector wavefield u in the isotropic medium can be decomposed into a curl-free P-wave wavefield $\mathbf{u}^{\mathrm{P}}$ and a divergence-free S-wave wavefield $\mathbf{u}^{\mathrm{S}}$. Combining the above relationship and the elastic wave equation, the decoupled P- and S-wave propagation equation can be expressed as:

$$\begin{cases} \ddot{\mathbf{u}} = V_{\mathrm{P}}^2 \nabla(\nabla\cdot\mathbf{u}) - V_{\mathrm{S}}^2 \nabla\times\nabla\times\mathbf{u}, \\ \ddot{\mathbf{u}}^{\mathrm{P}} = V_{\mathrm{P}}^2 \nabla(\nabla\cdot\mathbf{u}), \\ \mathbf{u}^{\mathrm{S}} = \mathbf{u} - \mathbf{u}^{\mathrm{P}}, \end{cases} \tag{1}$$

where $\ddot{\mathbf{u}}$ is the second-order time derivative of the vector displacement wavefield $\mathbf{u}$. Where V_{P} and V_{S} are the P- and S-wave velocities. ∇, $\nabla\cdot$, and $\nabla\times$ are the gradient, divergence, and curl operators, respectively. To reduce potential numerical dispersion caused by low S-wave velocity, we use the first-order stress-particle-velocity elastic wave equation (Wang and McMechan, 2015) from Eq. (1) to construct source and receiver vector wavefields.

Using the Poynting vector and the dipping angles, we calculated the propagation direction $\alpha(\mathbf{x})$ of the wavefield at the imaging point $\mathbf{x}$. Here, the propagation direction refers to the direction perpendicular to the wavefront propagating to imaging point $\mathbf{x}$. To obtain scalar images using the P- and S-wave vector wavefields, the reflectivity coefficient-based imaging theory (Wang and McMechan, 2015) and the cross-correlation imaging theory (Wang et al., 2016; Du et al., 2017; Zhou et al., 2019) have been proposed. Wang and McMechan (2015) proposed the vector-based (VB) prestack imaging condition to calculate scalar imaging results. This imaging condition can generate high-quality elastic images for representing reflection coefficient information. However, for complex subsurface wavefields and noises, it is difficult to accurately calculate the arrival time for each spatial point, leading to the possibility of noise points and discontinuous events in the imaging results.

The imaging conditions, such as the dot-product imaging condition, using the vector wavefields based on the cross-correlation imaging theory are more stable and easier to implement. For computing angles to generate ADCIGs using common-shot ERTM, only one angle with the main contribution to each imaging point is usually collected in imaging of primaries. The above angle computing method is referred to as a one-shot, one-position, and one-angle mapping strategy. Therefore, the dot-product imaging conditions using a one-shot, one-position, and one-angle mapping strategy for calculating PP and PS angle gathers can be expressed as follows in the angle domain (Vyas et al., 2011):

$$\begin{cases} I_{\mathrm{PP\_AG}}(\mathbf{x},\alpha) = \delta[\alpha_{\mathrm{s}}(\mathbf{x})-\alpha] \displaystyle\int \boldsymbol{v}_{\mathrm{P}}^{\mathrm{src}}(\mathbf{x};t)\cdot\boldsymbol{v}_{\mathrm{P}}^{\mathrm{rec}}(\mathbf{x};T-t)\mathrm{d}t, \\ I_{\mathrm{PS\_AG}}(\mathbf{x},\alpha) = \delta[\alpha_{\mathrm{s}}(\mathbf{x})-\alpha] \displaystyle\int \boldsymbol{v}_{\mathrm{P}}^{\mathrm{src}}(\mathbf{x};t)\cdot\boldsymbol{v}_{\mathrm{S}}^{\mathrm{rec}}(\mathbf{x};T-t)\mathrm{d}t, \end{cases} \tag{2}$$

where $I_{\mathrm{PP\_AG}}$ and $I_{\mathrm{PS\_AG}}$ are the PP and PS angle gathers, respectively. The symbol δ represents the Dirac delta function, equivalent to the binning process. The function $\alpha_{\mathrm{s}}(\mathbf{x})$ is the calculated incident angle based on a one-shot, one-position, and one-angle mapping strategy at the location of $\mathbf{x}$ using one shot gather, and α is the binning angle (the angle associated with the desired output angle range or sector). The variable t is the wavefield propagation time, and T is the maximum extrapolation time for migration. Similarly, $\boldsymbol{v}$ is the particle velocity, which corresponds also to $\{v_x, v_z\}$ in the 2D case. To be more concise, v_x and v_z are the horizontal and vertical particle-velocity components. The superscripts src and rec represent the source and receiver wavefields, respectively. And the subscripts P and S represent the P- and S-waves, respectively.

One of the primary objectives in calculating angle gathers is to obtain reflection coefficients that vary with propagation angles, thereby providing a foundation for AVA analysis. Next, we will derive the relationship between Eq. (2) and elastic wave reflection coefficients.

According to the definition of the dot-product operator, Eq. (2) can be rewritten as

$$\begin{cases} I_{\mathrm{PP\_AG}}(\mathbf{x},\alpha) = \delta[\alpha_{\mathrm{s}}(\mathbf{x})-\alpha]\cos[\theta_{\mathrm{PP}}(\mathbf{x})] \displaystyle\int \left|\boldsymbol{v}_{\mathrm{P}}^{\mathrm{src}}(\mathbf{x};t)\right|\left|\boldsymbol{v}_{\mathrm{P}}^{\mathrm{rec}}(\mathbf{x};T-t)\right|\mathrm{d}t, \\ I_{\mathrm{PS\_AG}}(\mathbf{x},\alpha) = \delta[\alpha_{\mathrm{s}}(\mathbf{x})-\alpha]\cos[\theta_{\mathrm{PS}}(\mathbf{x})] \displaystyle\int \left|\boldsymbol{v}_{\mathrm{P}}^{\mathrm{src}}(\mathbf{x};t)\right|\left|\boldsymbol{v}_{\mathrm{S}}^{\mathrm{rec}}(\mathbf{x};T-t)\right|\mathrm{d}t, \end{cases} \tag{3}$$

where $\theta_{\mathrm{PP}}(\mathbf{x})$ is the opening angle between the vibration direction of $\boldsymbol{v}_{\mathrm{P}}^{\mathrm{src}}$ and $\boldsymbol{v}_{\mathrm{P}}^{\mathrm{rec}}$ at the location of $\mathbf{x}$, and is geometrically equal to $2\alpha_{\mathrm{s}}(\mathbf{x})$. $\theta_{\mathrm{PS}}(\mathbf{x})$ is the opening angle between the vibration direction of $\boldsymbol{v}_{\mathrm{P}}^{\mathrm{src}}$ and $\boldsymbol{v}_{\mathrm{S}}^{\mathrm{rec}}$ at the location of $\mathbf{x}$, and is equal to $\alpha_{\mathrm{s}}(\mathbf{x})+\beta_{\mathrm{s}}(\mathbf{x})$. $\beta_{\mathrm{s}}(\mathbf{x})$ represents the reflection angle of S-wave at the location of $\mathbf{x}$. In practice, $\beta_{\mathrm{s}}(\mathbf{x})$ does not need to be computed explicitly when computing $\theta_{\mathrm{PS}}(\mathbf{x})$. Instead, $\theta_{\mathrm{PS}}(\mathbf{x})$ can be directly determined from the Poynting vectors of the source-side P-wave and the receiver-side S-wave. The symbol $|\cdot|$ denotes the modulus of a vector. According to the definition of reflection coefficients, the PP or PS reflection coefficients can be calculated using the magnitude of the receiver P- or S- wave particle velocity divided by the source P-wave magnitude (Claerbout, 1971; Sheriff and Geldart, 1995; Wang and McMechan, 2015). Therefore, the PP and PS reflection coefficients at each propagation time can be expressed as

$$\begin{cases} R_{\mathrm{PP}}(\mathbf{x},\alpha) = \mathrm{sgn}_{\mathrm{PP}}(\mathbf{x},\alpha)\dfrac{\left|\boldsymbol{v}_{\mathrm{P}}^{\mathrm{rec}}(\mathbf{x};T-t_{\mathrm{d}})\right|}{\left|\boldsymbol{v}_{\mathrm{P}}^{\mathrm{src}}(\mathbf{x};t_{\mathrm{d}})\right|}, \\ R_{\mathrm{PS}}(\mathbf{x},\alpha) = \mathrm{sgn}_{\mathrm{PS}}(\mathbf{x},\alpha)\dfrac{\left|\boldsymbol{v}_{\mathrm{S}}^{\mathrm{rec}}(\mathbf{x};T-t_{\mathrm{d}})\right|}{\left|\boldsymbol{v}_{\mathrm{P}}^{\mathrm{src}}(\mathbf{x};t_{\mathrm{d}})\right|}, \end{cases} \tag{4}$$

where R_{PP} and R_{PS} are the PP and PS reflection coefficients, respectively. The expression $\mathrm{sgn}_{\mathrm{PP}}(\mathbf{x},\alpha)$ is the polarity of a PP reflection at the location $\mathbf{x}$ for the imaging angle α, and $\mathrm{sgn}_{\mathrm{PS}}(\mathbf{x},\alpha)$ is the polarity of a PS reflection at the location $\mathbf{x}$ for the imaging angle α. t_{d} is the first arrival time on the source wavefield $\boldsymbol{v}_{\mathrm{P}}^{\mathrm{src}}(\mathbf{x};t)$. However, picking the exact first arrival time is not simple due to the complex propagation wavefields and noises. In practice, the picking uncertainty can be non-negligible and may significantly affect the stability of the extracted amplitudes. In particular, the picked arrival may deviate from the true reflection event for complex boundaries, such as fault interfaces and salt boundaries. Therefore, we still use the cross-correlation of the source and receiver wavefields at location $\mathbf{x}$ as the final imaging result. Following the above imaging rule, by combining Eqs. (3) and (4) while using the time integration of the wavefield at each moment, Eq. (3) can be rewritten as

$$\begin{cases} I_{\mathrm{PP\_AG}}(\mathbf{x},\alpha) = R_{\mathrm{PP}}(\mathbf{x},\alpha)\dfrac{\cos[\theta_{\mathrm{PP}}(\mathbf{x})]}{\mathrm{sgn}_{\mathrm{PP}}(\mathbf{x},\alpha)}\delta[\alpha_{\mathrm{S}}(\mathbf{x})-\alpha]\displaystyle\int\left|\boldsymbol{v}_{\mathrm{P}}^{\mathrm{src}}(\mathbf{x};t)\right|^2\mathrm{d}t, \\ I_{\mathrm{PS\_AG}}(\mathbf{x},\alpha) = R_{\mathrm{PS}}(\mathbf{x},\alpha)\dfrac{\cos[\theta_{\mathrm{PS}}(\mathbf{x})]}{\mathrm{sgn}_{\mathrm{PS}}(\mathbf{x},\alpha)}\delta[\alpha_{\mathrm{S}}(\mathbf{x})-\alpha]\displaystyle\int\left|\boldsymbol{v}_{\mathrm{P}}^{\mathrm{src}}(\mathbf{x};t)\right|^2\mathrm{d}t. \end{cases} \tag{5}$$

According to Eq. (5), the angle-domain dot-product imaging conditions not only contain the PP and PS reflection coefficients but also involve the angle-dependent factors and the sign of the reflection polarity. Consequently, directly using the dot-product imaging condition to calculate imaging results using vector wavefields cannot yield imaging results that accurately reflect the reflection coefficient. Next, we will derive the corrected angle-domain dot-product imaging conditions to accurately represent the reflection coefficient used to correct the angle-dependent factors and the sign of the reflection polarity in conventional dot-product imaging.

2.2. The corrected angle-domain dot-product imaging condition

This section aims to derive new angle-domain imaging conditions to obtain improved AVA information. According to Eq. (5), it is relatively straightforward to get the corrected angle-domain imaging conditions by eliminating the angle-dependent factors and the sign of the reflection polarity:

$$\begin{cases} I_{\mathrm{PP\_AG}}^{\mathrm{cor}}(\mathbf{x},\alpha) = \dfrac{\mathrm{sgn}_{\mathrm{PP}}(\mathbf{x},\alpha)}{\cos[\theta_{\mathrm{PP}}(\mathbf{x})]}\delta[\alpha_{\mathrm{S}}(\mathbf{x})-\alpha]\displaystyle\int v_{\mathrm{P}}^{\mathrm{src}}(\mathbf{x};t)\cdot v_{\mathrm{P}}^{\mathrm{rec}}(\mathbf{x};T-t)\mathrm{d}t, \\ I_{\mathrm{PS\_AG}}^{\mathrm{cor}}(\mathbf{x},\alpha) = \dfrac{\mathrm{sgn}_{\mathrm{PS}}(\mathbf{x},\alpha)}{\cos[\theta_{\mathrm{PS}}(\mathbf{x})]}\delta[\alpha_{\mathrm{S}}(\mathbf{x})-\alpha]\displaystyle\int v_{\mathrm{P}}^{\mathrm{src}}(\mathbf{x};t)\cdot v_{\mathrm{S}}^{\mathrm{rec}}(\mathbf{x};T-t)\mathrm{d}t. \end{cases} \tag{6}$$

Although the angle gathers calculated using Eq. (6) can reflect reflection coefficients, calculating the angle between the vibration directions of vectors during migration is not a straightforward approach. Additionally, the polarity of the reflection for both PP and PS reflections at varying angles requires further determination. Therefore, it is necessary to derive their workable expressions. Given the distinct propagation characteristics of P- and S-waves, we will derive the corrected angle-domain dot-product imaging conditions individually for PP and PS imaging.

2.2.1. The corrected angle-domain dot-product imaging condition for PP imaging

The imaging conditions in Eq. (6) contain the sign of a reflection polarity. For a given subsurface reflector at a fixed incidence angle with an unknown polarity, there are only two possible cases: positive or negative polarity. Once we derive the correction operators for the PP and PS imaging conditions in Eq. (6) under these two cases, we can obtain the final expression of the corrected dot-product imaging condition. Therefore, we provide derivations for the two possibilities of positive or negative reflection coefficients as shown in Fig. 1.

For P-waves, their propagation directions are parallel to the vibration directions. When the reflection coefficient at the incident angle α is greater than zero, we can get $\mathrm{sgn}_{\mathrm{PP}}(\mathbf{x},\alpha)=1$ and $\theta_{\mathrm{PP}}=2\alpha$ as shown in Fig. 1(a). In this scenario, the weight factor $\mathrm{sgn}_{\mathrm{PP}}(\mathbf{x},\alpha)/\cos[\theta_{\mathrm{PP}}(\mathbf{x})]$ can be rewritten as $1/\cos(2\alpha)$. When the reflection coefficient at the incident angle α is less than zero, the polarity of the reflection $\mathrm{sgn}_{\mathrm{PP}}(\mathbf{x},\alpha) = -1$. The distinction is that the vibration direction of the receiver vector wavefield experiences a 180° reversal relative to its propagation direction based on Eq. (4). According to Fig. 1(b), the angle between the source and receiver vector wavefield is equal to $\pi-2\alpha$. In this case, the weight factor $\mathrm{sgn}_{\mathrm{PP}}(\mathbf{x},\alpha)/\cos[\theta_{\mathrm{PP}}(\mathbf{x})]$ can still be expressed as $1/\cos(2\alpha)$. According to the above derivation, the resulting expression the PP imaging condition is the same regardless of whether the subsurface reflection coefficient is positive or negative. Furthermore, the above derivation shows that the final corrected condition only involves the cosine of the opening angle. Therefore, the polarity of the reflection coefficient is not required a priori. Additionally, to obtain dimensionless unit images reflecting the relatively correct reflection coefficient, we introduce the normalized by source illumination (Kaelin and Guitton, 2006) to the imaging condition. Therefore, the corrected angle-domain dot-product imaging condition for PP imaging is

$$I_{\mathrm{PP\_AG}}^{\mathrm{cor}}(\mathbf{x},\alpha) = \frac{\delta[\alpha_{\mathrm{S}}(\mathbf{x})-\alpha]\int v_{\mathrm{P}}^{\mathrm{src}}(\mathbf{x};t)\cdot v_{\mathrm{P}}^{\mathrm{rec}}(\mathbf{x};T-t)\mathrm{d}t}{\cos(2\alpha)\int v_{\mathrm{P}}^{\mathrm{src}}(\mathbf{x};t)\cdot v_{\mathrm{P}}^{\mathrm{src}}(\mathbf{x};t)\mathrm{d}t}. \tag{7}$$

Due to the introduction of angle-dependent operators for correcting the conventional dot-product imaging condition, the absence of amplitudes occurs in PP angle gathers calculated using Eq. (7) at 45°. To mitigate this issue, we recover the amplitudes around the opening angle in Eq. (7) using a combination of regularization written as follows:

$$I_{\mathrm{PP\_AG}}^{\mathrm{cor}}(\mathbf{x},\alpha) = \frac{\delta[\alpha_{\mathrm{S}}(\mathbf{x})-\alpha]\cos(2\alpha)\int v_{\mathrm{P}}^{\mathrm{src}}(\mathbf{x};t)\cdot v_{\mathrm{P}}^{\mathrm{rec}}(\mathbf{x};T-t)\mathrm{d}t}{\left[\cos^2(2\alpha)+\varepsilon\right]\int v_{\mathrm{P}}^{\mathrm{src}}(\mathbf{x};t)\cdot v_{\mathrm{P}}^{\mathrm{src}}(\mathbf{x};t)\mathrm{d}t}, \tag{8}$$

where ε is the regularization parameter. By setting an angular threshold of 3° in opening angle and constrain the correction error to within 3%, the regularization parameter ranges of $\varepsilon\in\left[1.0\times10^{-5}, 5.0\times10^{-4}\right]$. In addition, we apply a smoothing taper along the angle-direction at each depth and employ a large smoothing

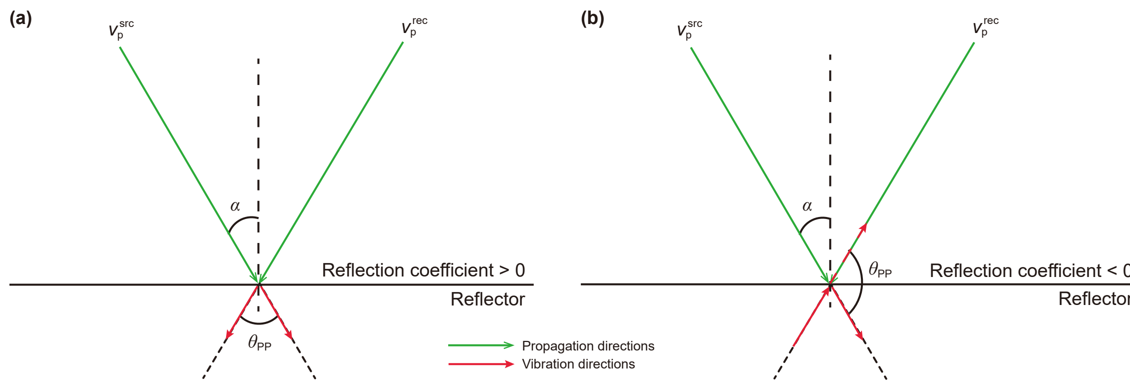

Fig. 1. Kinematic example of PP particle motions when a reflection coefficient is positive **(a)** and negative **(b)**. The green lines represent the propagation directions of P-waves, and the red lines represent the vibration directions of P-waves. α is the calculated incident angle using the Poynting vectors, and θ_{PP} is the opening angle of the vibration directions.

window within the incidence angle range of 43° to 47° interval to ensure amplitude continuity across the transition.

2.2.2. The corrected angle-domain dot-product imaging condition for PS imaging

For the PS imaging condition, we still need to consider the influence of the sign of the reflection coefficient on the vibration direction of the vector wavefield. Unlike the P-wave wavefield, the vibration direction of S-waves is perpendicular to the propagation direction. We define that the direction points outside perpendicular to the vertical plane (Du et al., 2014). Therefore, the vibration direction of the S-wave is shown by red lines in Fig. 2.

According to Fig. 2(a), when the sign of the reflection polarity $\mathrm{sgn}_{\mathrm{PS}}(\mathbf{x},\alpha)$ is equal to 1 at the incident angle α, the angle θ_{PS} equals to $\pi/2+\alpha+\beta$. In this case, the weight factor $\mathrm{sgn}_{\mathrm{PS}}(\mathbf{x},\alpha)/\cos[\theta_{\mathrm{PS}}(\mathbf{x})]$ of the PS angle-domain imaging condition in Eq. (6) can be rewritten as $-1/\sin(\alpha+\beta)$. When $\mathrm{sgn}_{\mathrm{PS}}(\mathbf{x},\alpha)$ equals to -1, the direction points inside perpendicular to the vertical plane and the vibration direction of S-waves changes as shown in Fig. 2(b). The angle θ_{PS} equals to $\pi/2-\alpha-\beta$, and the weight factor $\mathrm{sgn}_{\mathrm{PS}}(\mathbf{x},\alpha)/\cos[\theta_{\mathrm{PS}}(\mathbf{x})]$ remains as $-1/\sin(\alpha+\beta)$. As shown by the above derivation, the corrected dot-product imaging condition for PS imaging also depends only on the angle-dependent correction operator and does not require prior knowledge of the polarity of the subsurface reflection coefficient. Then, the corrected angle-domain dot-product imaging condition with the normalized by source illumination for PS imaging is

$$I_{\mathrm{PS\_AG}}^{\mathrm{cor}}(\mathbf{x},\alpha)=\frac{-\delta[\alpha_{\mathrm{S}}(\mathbf{x})-\alpha]\int v_{\mathrm{P}}^{\mathrm{src}}(\mathbf{x};t)\cdot v_{\mathrm{S}}^{\mathrm{rec}}(\mathbf{x};T-t)\mathrm{d}t}{\sin(\alpha+\beta)\int v_{\mathrm{P}}^{\mathrm{src}}(\mathbf{x};t)\cdot v_{\mathrm{P}}^{\mathrm{src}}(\mathbf{x};t)\mathrm{d}t}. \tag{9}$$

Because Eq. (8) performs angle-dependent correction based on the PS opening angle, computing the PS opening angle is more direct and implementation-consistent with the correction operator. Here, we calculate the PS opening angle by computing the source-side P-wave and the receiver-side S-wave Poynting vectors and evaluate the opening angle by an inverse cosine (Yoon and Marfurt, 2006).

For PS imaging, an amplitude deficiency is also observed near the incident angle of 0°. Due to a vertically incident P-wave does not generate a converted S-wave component, we handle this case by imposing an angle restriction. Therefore, we restrict the incidence angle to ≥5° avoid unstable correction near the incident angle of 0°. Using Eqs. (8) and (9), we can get improved AVA information by outputting PP and PS angle gathers.

Because the corrected dot-product imaging condition introduces an angle-dependent corrector operator, it inevitably incurs additional computational overhead compared with the standard ERTM workflow. First is Poynting vector calculation. The incident and reflection angles at each spatial location for each shot are computed by evaluating the Poynting vectors on the source and receiver sides. Relative to wavefield propagation, this step mainly consists of spatial dot products of wavefield components, and the associated cost is therefore relatively small. The second source of overhead comes from angle binning to generate the

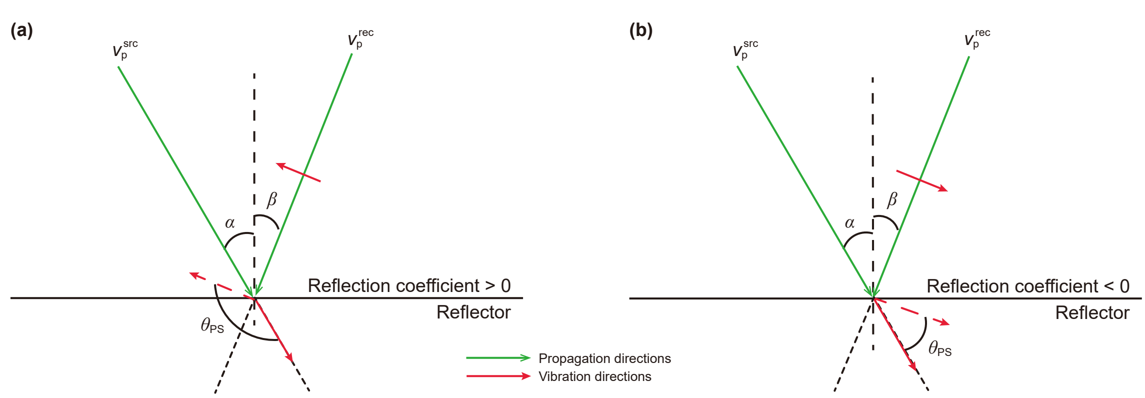

Fig. 2. Kinematic example of PS particle motions when a reflection coefficient is positive **(a)** and negative **(b)**. The green lines represent the propagation directions of P- and S-waves and the red lines represent the vibration directions of P- and S-waves. α is the calculated incident angle using the Poynting vectors, θ_{PS} is the opening angle of the vibration directions, and β is the reflection angle.

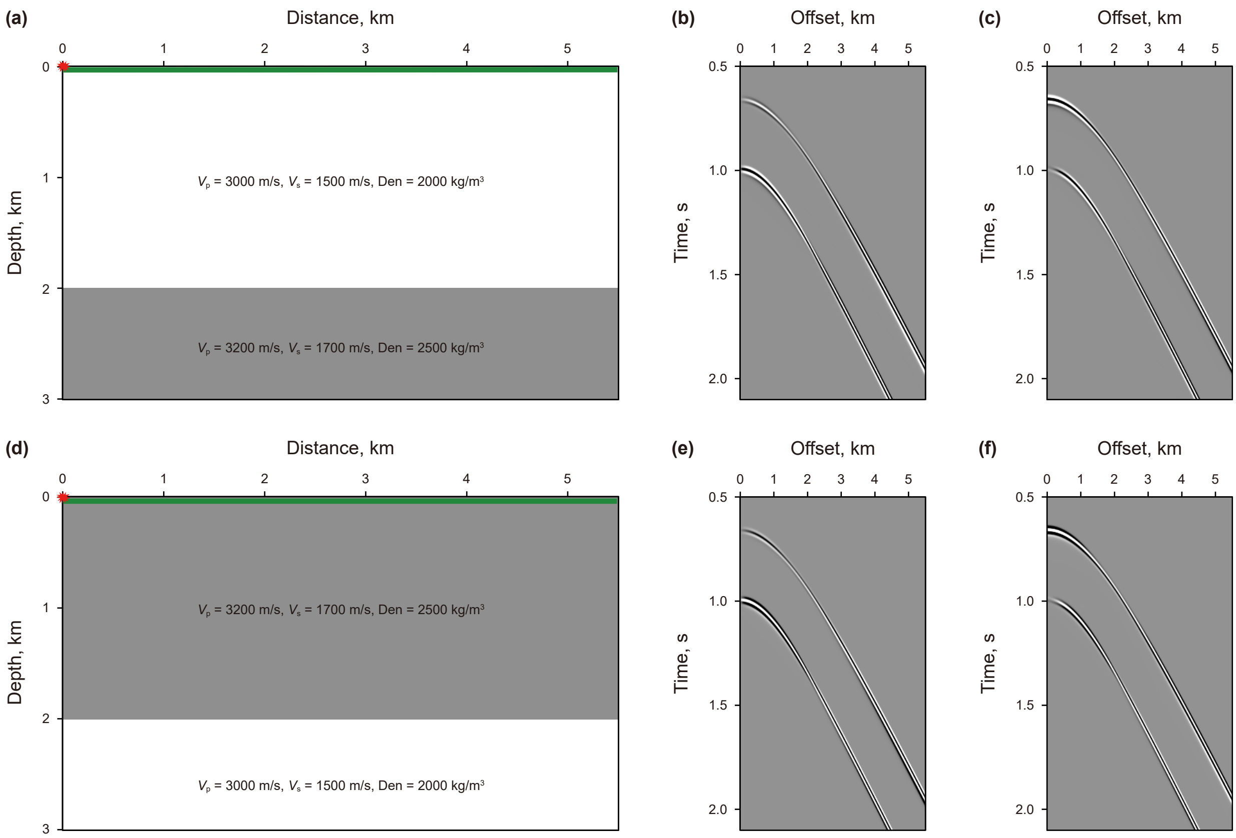

Fig. 3. **(a)**, **(d)** The two-layer models with different velocities. **(b)** and **(c)** are the simulated lateral and vertical component shot gathers using the model in Fig. 3(a). **(e)** and **(f)** are the simulated lateral and vertical component shot gathers utilizing the model in Fig. 3(d) The red explosion symbols represent the source locations, and the green lines represent the receivers.

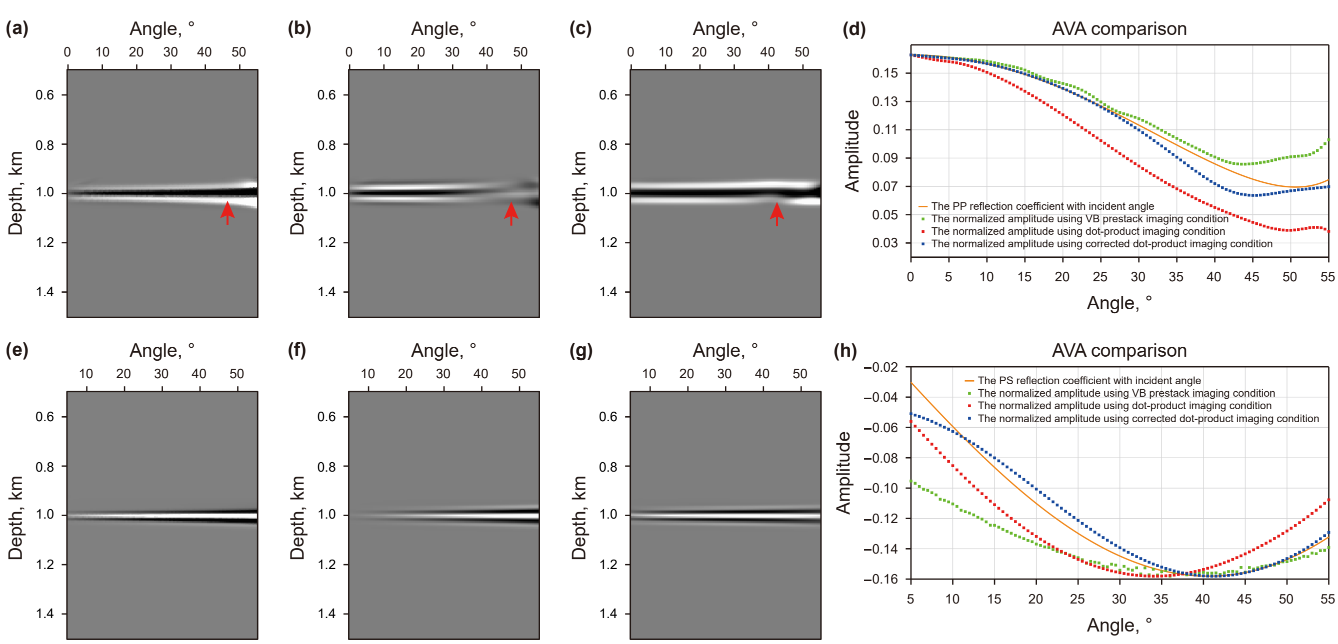

Fig. 4. **(a)**–**(c)** The PP angle gathers using the VB prestack, conventional and corrected imaging-domain dot-product imaging conditions, respectively. **(d)** The comparison between the amplitudes extracted from the PP angle gathers and the theoretical PP reflection coefficient. **(e)**–**(g)** The PS angle gathers using the VB prestack, conventional and corrected imaging-domain dot-product imaging conditions, respectively. We multiply the amplitudes of the original PS angle gather by -1 to make sure the direction points inside perpendicular to the vertical plane. **(h)** The comparison between the amplitudes extracted from PS angle gathers and the theoretical PS reflection coefficient. The angle gathers are calculated with a binning resolution of 0.5°, and the red arrow indicates the imaging at 45° in the PP angle gathers.

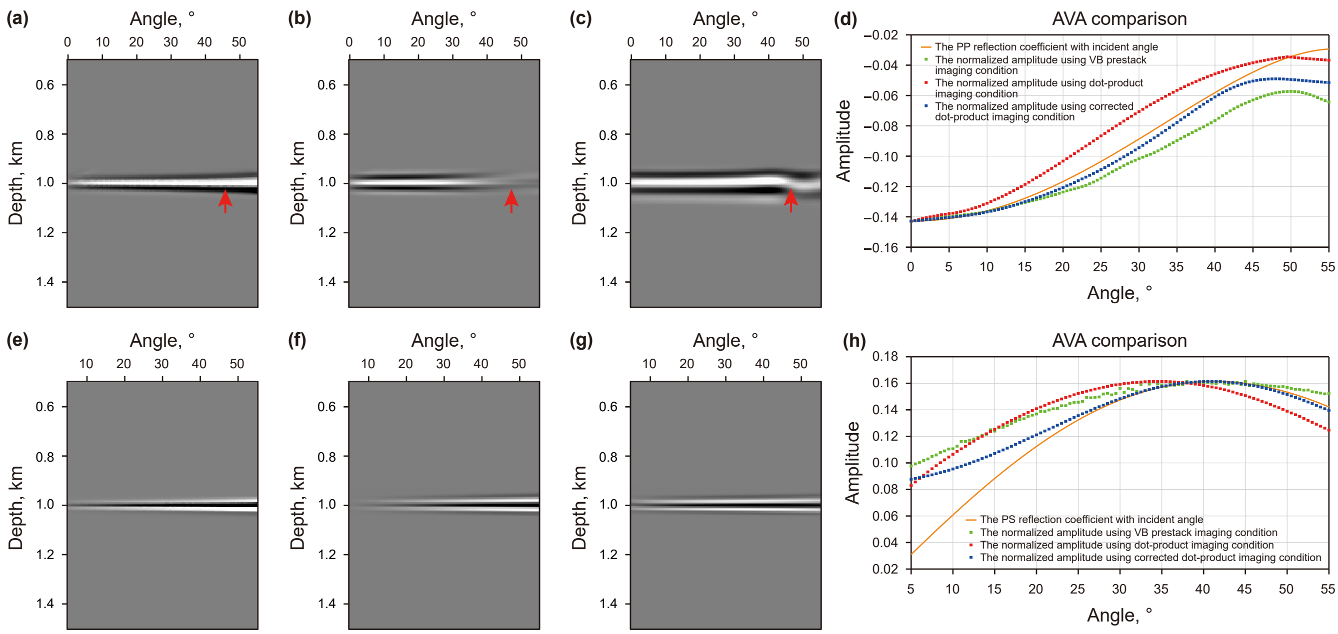

Fig. 5. **(a)**–**(c)** The PP angle gathers using the VB prestack, conventional and corrected imaging-domain dot-product imaging conditions, respectively. **(d)** The comparison between the amplitudes extracted from the PP angle gathers and the theoretical PP reflection coefficient. **(e)**–**(g)** The PS angle gathers using the VB prestack, conventional and corrected imaging-domain dot-product imaging conditions, respectively. We multiply the amplitudes of the original PS angle gather by −1 to make sure the direction points inside perpendicular to the vertical plane. **(h)** The comparison between the amplitudes extracted from PS angle gathers and the theoretical PS reflection coefficient. The angle gathers are calculated with a binning resolution of 0.5°, and the red arrow indicates the imaging at 45° in the PP angle gathers.

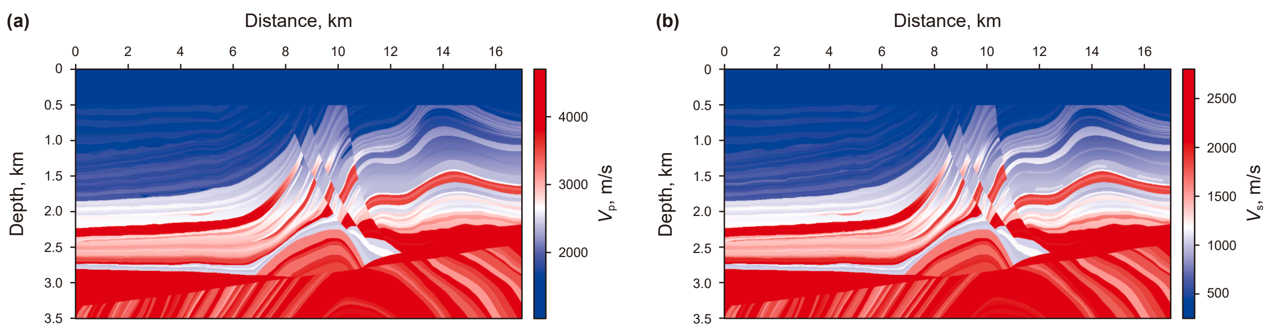

Fig. 6. **(a)** The stratigraphy P-wave velocity model for simulating shot gathers. **(b)** The smoothed P-wave velocity model for implementing migration.

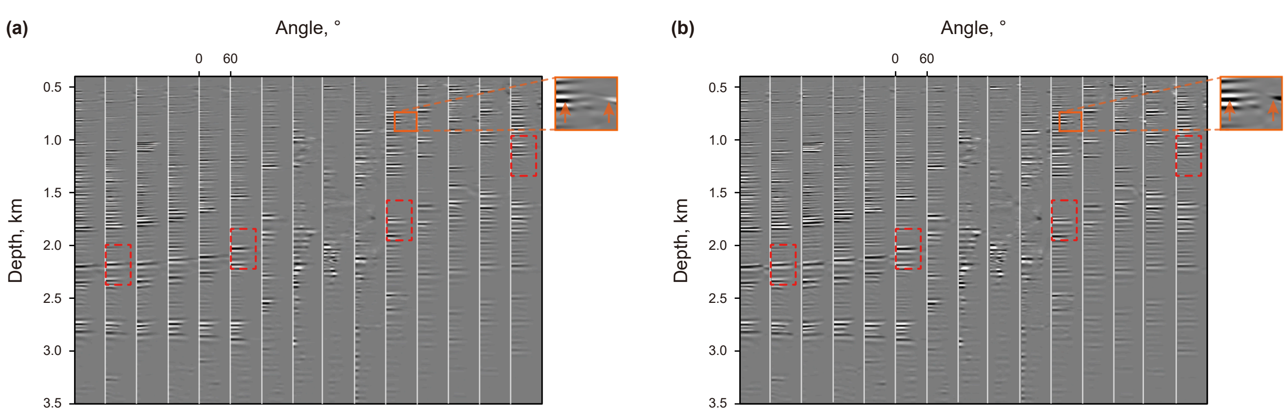

Fig. 7. **(a)** The PP angle gathers using the conventional angle-domain dot-product imaging condition. **(b)** The PP angle gathers using the correct angle-domain dot-product imaging condition. The orange boxes are marked for the enlarged areas, and the orange arrows indicate the imaging near the reflection angle of 45°. We select three events with a wide-range imaging angle and mark them with red dotted box.

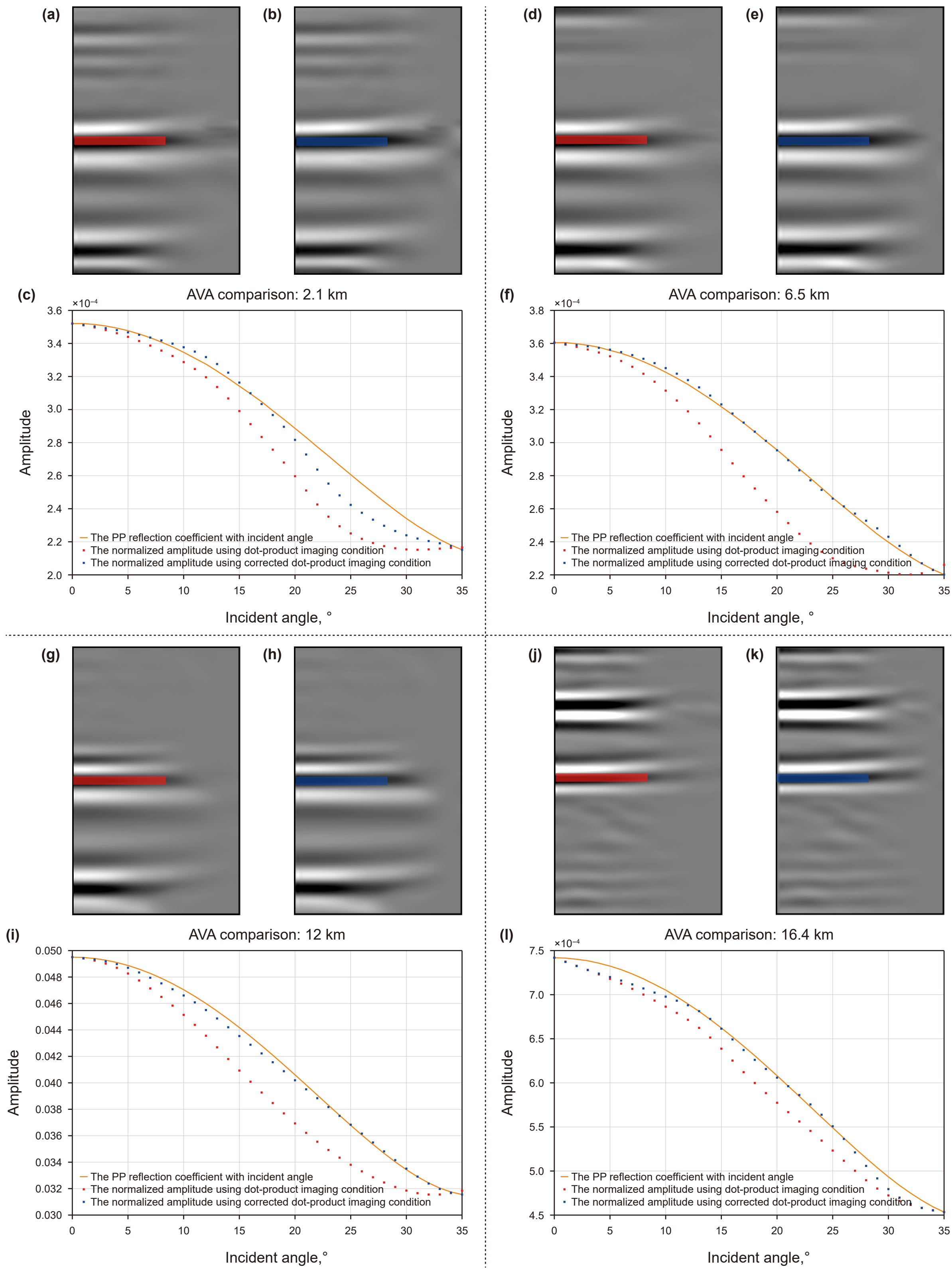

Fig. 8. **(a)**–**(b)**, **(d)**–**(e)**, **(g)**–**(h)** and **(j)**–**(k)** are enlarged images of the PP angle gathers located at 2.1, 6.5, 12, and 16.4 km, respectively. **(a)**, **(d)**, **(g)** and **(j)** represent the PP angle gathers computed using the conventional dot-product imaging condition, while **(b)**, **(e)**, **(h)** and **(k)** depict the PP angle gathers computed using the corrected dot-product imaging condition. The imaging events to be compared are marked with red and blue lines, respectively. The comparison between the normalized amplitudes of the marked events with the theoretical reflection coefficients are shown in **(c)**, **(f)**, **(i)** and **(l)**.

ADCIGs by applying the angle-dependent operator. Calculating ADCIGs differs from the standard stacking strategy. Instead of accumulating the images into a single value at each image point, the contributions are sorted in imaging angle bins, which increases memory consumption and introduces extra computation. As a result, applying the corrected dot-product imaging condition does require additional running time. Nevertheless, this extra cost is justified by the richer AVA information provided by the angle-domain outputs. The additional expense introduced by angle binning can be mitigated in two ways. On the one hand, the angle binning can be accelerated using high-performance parallelization strategies such as OpenMP and MPI. On the other hand, the computational load can be reduced by imposing an angle range limit during sorting, for example by restricting the maximum output angle of the ADCIGs. Next, we use simple models to verify the accuracy of proposed imaging conditions.

2.3. Angle gathers using two-layer models

The two-layer models are shown in Fig. 3(a), (d). The models contain 1001 (horizontal) × 301 (vertical) grid points, and the grid space is 5 m. We designed two sets of distinct velocity models to validate the proposed imaging conditions for accuracy under different reflection coefficients. For the model in Fig. 3(a), the P-wave and S-wave velocities (V_p and V_s) of the first layer are denoted as 3000 and 1500 m/s, the P- and S-wave velocities of the second layer as 3200 and 1700 m/s. The density (Den) of the first layer is 2000 kg/m^3, and the density of the second layer is 2500 kg/m^3. For the other model as shown in Fig. 3(b), the P-wave and S-wave velocities of the first layer are 3200 and 1700 m/s, and the P-wave and S-wave velocities of the second layer are 3000 and 1500 m/s. The density of the first layer is 2500 kg/m^3, and the density of the second layer is 2000 kg/m^3.

To simulate the shot gathers, the source and receivers are both located at the surface, and each receiver is responsible for receiving seismic data to ensure that as small angles as possible are imaged. Each source location is deployed at the far left of the model, and the shot interval is 5 m for generating enough imaging angles. The decoupled elastic wave equation in Eq. (1) and a Ricker wavelet with a peak frequency of 30 Hz are used to simulate shot gathers. The shot gathers simulated using the first model set are shown in Fig. 3(b) and (c), while those simulated using the second model set are shown in Fig. 3(e) and (f).

To demonstrate the advantages of the proposed imaging conditions and the difference in calculating angle gathers with the VB prestack imaging conditions proposed by Wang and McMechan (2015). We calculate angle gathers using the VB prestack imaging condition, the conventional dot-product, and the proposed imaging conditions. The calculated PP and PS angle gathers using the two-layer model in Fig. 3(a) are shown in Fig. 4. Considering the imaging amplitudes may be influenced by the critical angles and angle-dependent reflection coefficients, we display the PP and PS angle gathers with the maximum angle of 55°. Since there is no waveform conversion at normal incident angles, we show that the PS angle gathers from 5°. Additionally, even with a uniform surface receiver spacing, the angular illumination at a given subsurface image point is generally non-uniform. Therefore, a straight accumulation of the backpropagated receiver wavefield in angle bins can indeed introduce amplitude imbalance in calculating angle gathers. This imbalance is primarily a consequence of non-uniform subsurface illumination, rather than a physical AVA effect. To remove illumination imprint from the angle-dependent amplitudes, we explicitly compute an angle-illumination weight using a Gaussian-weighted binning strategy at each image point and apply it to the final ADCIGs.

We extract the amplitudes at 1 km depth from the PP and PS angle gathers to quantitatively compare the relationship between amplitude values and theoretical reflection coefficients. We normalize these extracted amplitudes and compare them to theoretical reflection coefficients, as shown in Fig. 4(c), (f).

Comparing Fig. 4(a) and (b) (or (c)), the PP angle gather calculated using the VB prestack imaging condition has continuous imaging events. This is because the VB prestack imaging condition does not contain an angle-dependent factor. However, the angle gather in Fig. 4(a) suffers from imaging noises due to potential inaccuracies in the excitation amplitude calculations. Comparing Fig. 4(b) and (c), the PP angle gather using the corrected imaging condition has the same amplitude polarity even though incident angles are greater than 45° as marked by the red arrows. This is because the angle-dependent complement factor in the corrected imaging condition corrects the polarity reversal problem. According to Fig. 4(d), the normalized amplitudes from the PP angle gather in Fig. 4(a), (c) match the theoretical reflection coefficients better. However, the normalized amplitudes calculated using the VB prestack imaging condition exhibit strong oscillations due to the imaging noises, while the imaging amplitudes in Fig. 4(c) are more continuous.

For the PS angle gathers in Fig. 4(e)–(g), the PS angle gathers all have great imaging event consistency. However, the PS angle gather calculated using the conventional imaging condition has

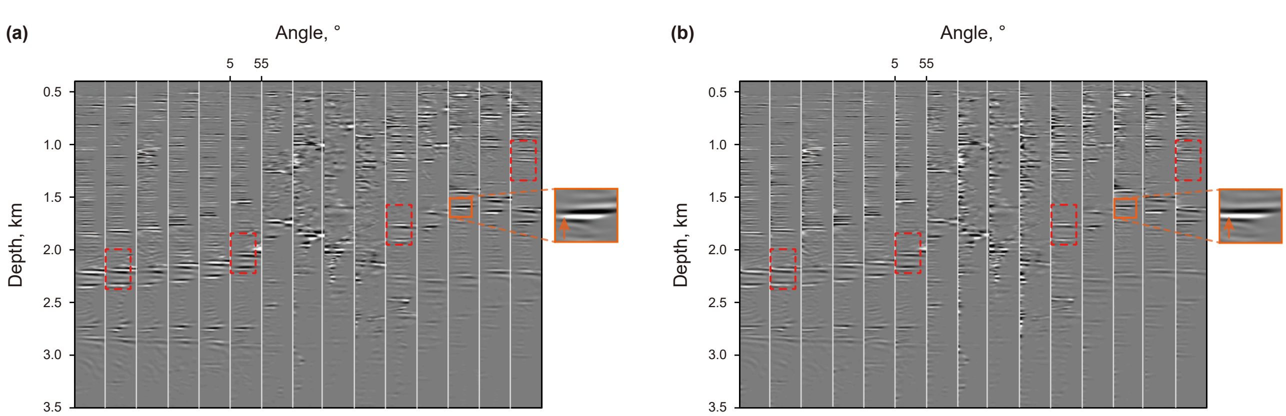

Fig. 9. **(a)** The PS angle gathers using the conventional angle-domain dot-product imaging condition. **(b)** The PS angle gathers using the correct angle-domain dot-product imaging condition. The orange boxes are marked for the enlarged areas, and the orange arrows indicate the imaging near the reflection angle 5°. We select three events with a wide-range imaging angle and mark them with red dotted box.

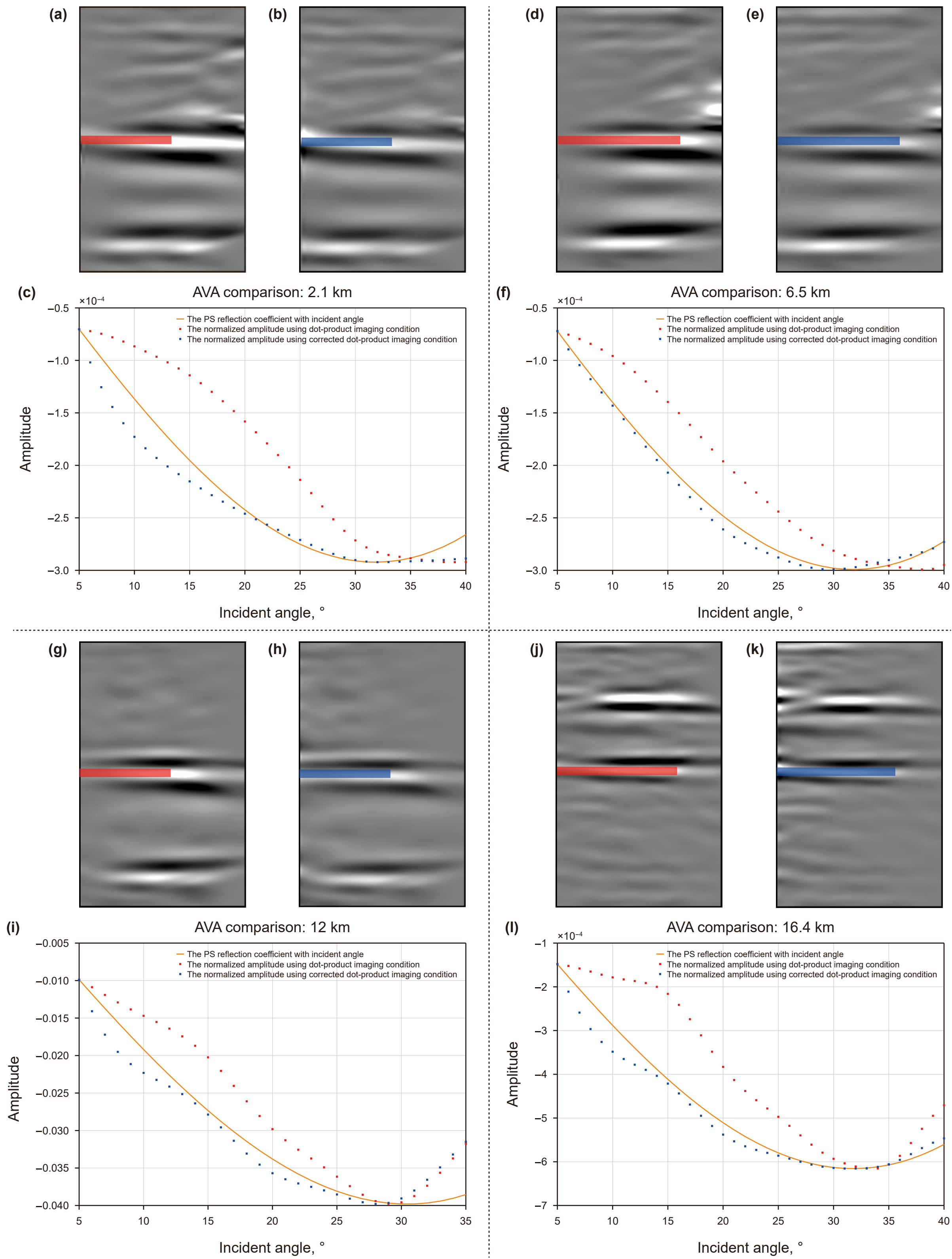

Fig. 10. **(a)**–**(b)**, **(d)**–**(e)**, **(g)**–**(h)** and **(j)**–**(k)** are enlarged images of the PS angle gathers located at 2.1, 6.5, 12, and 16.4 km, respectively. **(a)**, **(d)**, **(g)** and **(j)** represent the PS angle gathers computed using the conventional dot-product imaging condition, while **(b)**, **(e)**, **(h)** and **(k)** depict the PS angle gathers computed using the corrected dot-product imaging condition. The imaging events to be compared are marked with red and blue lines, respectively. The comparison between the normalized amplitudes of the marked events with the theoretical reflection coefficients are shown in **(c)**, **(f)**, **(i)** and **(l)**.

smaller amplitude values at small angles, as shown in Fig. 4(h) for the incident angle from 5° to 20°. The amplitudes at small angles calculated using the corrected imaging condition for PS angle gathers are effectively compensated. Additionally, the normalized amplitudes from Fig. 4(e), (g) still match the PS reflection coefficient better, except that the continuity of the imaging amplitudes in Fig. 4(e) is poorer.

Next, we show the angle gathers and AVA information comparison using the two-layer model in Fig. 3(d).

Fig. 5(a)–(c) show the PP angle gathers calculated using the VB prestack, the conventional, and the corrected angle-domain dot-product imaging conditions, respectively. Fig. 5(e)–(g) show the PS angle gathers computed using the VB prestack, the conventional, and the corrected angle-domain dot-product imaging conditions, respectively. According to Fig. 5, the imaging events calculated using the VB prestack and corrected dot-product imaging conditions show better amplitude consistency, and their normalized amplitude curves also exhibit better marching with the theoretical reflection coefficients. However, the imaging amplitudes calculated using the VB prestack imaging conditions exhibit strong oscillations.

3. Numerical examples

This section uses a subset of the Marmousi2 model (Martin et al., 2006) to validate the accuracy and robustness of the proposed imaging conditions in calculating improved AVA information.

The Marmousi2 model used has 3201 grid points in the horizontal direction and 401 grid points in the vertical direction. The stratigraphy P-wave velocity model for simulating shot gathers is shown in Fig. 6(a), and the smoothed P-wave velocity model for implementing migration is shown in Fig. 6(b). The S-wave velocity model is obtained by dividing the P-wave velocity model by 1.73. And the density is set to a constant value of 2000 kg/m^3.

Employing a finite-difference method based on the decoupled elastic wave equation, we use an impulse wavelet with a 25 Hz dominant frequency to excite the P-wave source and simulate 500 shot gathers. The shot interval is 30 m, and the receivers are spaced 5 m. The minimum and maximum offsets are 0 m and 7 km. The shot gathers are recorded using a both-side receiver approach, with a maximum recording time of 5 s. We extracted 15 horizontal locations to display angle gathers. The first angle gather is located at a horizontal location of 1000 m, followed by showing angle gathers at intervals of 1100 m. The angle range for each PP angle gather is from 0° to 60°, while for each PS angle gather is from 5° to 60° considering no wave conversion at 0°.

Fig. 7 shows the PP angle gathers for the partial Marmousi2 model, where Fig. 7(a) is the PP angle gathers calculated using the conventional imaging condition, and Fig. 7(b) is the PP angle gathers calculated using the proposed imaging condition. The angle gathers all show high-quality imaging, according to Fig. 7. Comparing the enlarged areas in Fig. 7(a) and (b), the imaging amplitudes computed using the corrected imaging condition exhibit more consistent polarity beyond 45°.

Considering the range and coverage of imaging angles in the angle gathers, we selected four different imaging locations for comparing amplitude curves. Fig. 8(a), (d), (g) and (j) show the PP angle gathers computed using the conventional dot-product imaging condition, while Fig. 8(b), (e), (h) and (k) depict the PP angle gathers computed using the corrected dot-product imaging condition. The comparison between the normalized amplitudes of the marked events with the theoretical reflection coefficients are shown in Fig. 8(c), (f), (i) and (l). According to the comparison of the amplitude curves in Fig. 8, the normalized amplitudes calculated using the corrected dot-product imaging condition exhibit a better match with the theoretical reflection coefficients.

Fig. 9(a), (b) show the PS angle gathers calculated using the conventional and corrected angle-domain dot-product imaging conditions, respectively. The PS angle gathers calculated using the corrected imaging condition exhibits more continuous imaging events, especially at small angles marked by the orange arrows in the enlarged area. This is primarily attributed to the correction introduced by the angle-dependent factors in Eq. (9).

To enhance the fairness of the comparison, we choose the same positions as in Fig. 8 for the comparison of the amplitude curves. Fig. 10(a), (d), (g) and (j) show the PP angle gathers computed using the conventional dot-product imaging condition, while Fig. 10(b), (e), (h) and (k) depict the PS angle gathers computed using the corrected dot-product imaging condition. The comparison between the normalized amplitudes of the marked events with the theoretical reflection coefficients are shown in Fig. 10(c), (f), (i) and (l). According to the comparison of the amplitude curves in Fig. 10, the normalized amplitudes using the corrected imaging condition still better match the theoretical reflection coefficients.

In summary, the angle gathers calculated using the corrected imaging conditions can better capture the variations of reflection coefficients with angles.

4. Conclusion

This paper lies in clarifying the physical significance of the conventional dot-product imaging conditions and proposing corrected dot-product imaging conditions that can represent the reflection coefficients based on the kinematic characteristics of the P- and S-waves. According to the derived relationship between the conventional angle-domain dot-product imaging conditions and the reflection coefficients, the imaging amplitudes calculated using the imaging conditions are related to the reflection coefficients, angle-dependent factors, and the signs of the reflection polarities. Based on the above relationship, we formulate imaging conditions that directly represent the reflection coefficients. Then, we derive the corrected angle-domain dot-product imaging conditions by analyzing the wavefield propagation kinematics when the reflection coefficient is positive and negative. To verify the accuracy of the proposed imaging conditions, we calculate the PP and PS angle gathers using simple models based on the VB prestack, the conventional and the corrected angle-domain dot-product imaging conditions. The results demonstrate that the corrected imaging conditions yield imaging amplitudes that closely align with theoretical reflection coefficients. The angle gathers for the complex model using the corrected imaging conditions better reflects the variations of reflection coefficients with angle. This improved AVA imaging based on the corrected imaging conditions validates the practicality of the proposed imaging conditions.

CRediT authorship contribution statement

Shu-Kui Zhang: Methodology. **Shao-Ping Lu:** Methodology. **Zhi-Jing Liu:** Methodology. **Han Wu:** Methodology. **Gang Fang:** Methodology.

Declaration of interests

The authors declare that they have no known competing financial interests or personal relationships that could have appeared to influence the work reported in this paper.

Acknowledgments

This study is partially funded by the National Key Research and Development Program of China (Grant No. 2024YFF0508202), the National Natural Science Foundation of China (Grant Nos. 42474137, 42504110), supported by the China Postdoctoral Science Foundation under Grant No. 2024M761810, and supported by open project fund of National Engineering Research Center of Digital Construction and Evaluation Technology of Urban Rail Transit 2024HWYQ-030.

References

Aki, K., Richards, P.G., 2002. Quantitative Seismology. MIT Press. https://doi.org/10.1785/gssrl.76.5.551.
Balch, A.H., Erdemir, C., 1994. Sign-change correction for prestack migration of P-S converted wave reflections. Geophys. Prospect. 42 (6), 637–663. https://doi.org/10.1111/j.1365-2478.1996.tb00144.x.
Chang, W.F., McMechan, G.A., 1987. Elastic reverse-time migration. Geophysics 52 (10), 1365–1375. https://doi.org/10.1190/1.1442249.
Chang, W.F., McMechan, G.A., 1994. 3-D elastic prestack, reverse-time depth migration. Geophysics 59 (4), 597–609. https://doi.org/10.1190/1.1443620.
Claerbout, J.F., 1971. Toward a unified theory of reflector mapping. Geophysics 36 (3), 467–481.
Du, Q.Z., Zhu, Y.T., Ba, J., 2012. Polarity reversal correction for elastic reverse time migration. Geophysics 77 (2), S31–S41. https://doi.org/10.1190/1.1440185.
Du, Q., Gong, X., Zhang, M., Zhu, Y., et al., 2014. 3D PS-wave imaging with elastic reverse-time migration. Geophysics 79 (5), S173–S184. https://doi.org/10.1190/geo2013-0253.1.
Du, Q., Guo, C., Zhao, Q., et al., 2017. Vector based elastic reverse time migration based on scalar imaging condition. Geophysics 82 (2), S111–S127. https://doi.org/10.1190/geo2016-0146.1.
Duan, Y., Sava, P., 2015. Scalar imaging condition for elastic reverse time migration. Geophysics 80 (4), S127–S136. https://doi.org/10.1190/geo2014-0453.1.
Gong, T., Nguyen, B.D., McMechan, G.A., 2016. Polarized wavefield magnitudes with optical flow for elastic angle-domain common-image gathers. Geophysics 81 (4), S239–S251. https://doi.org/10.1190/geo2015-0518.1.
Kaelin, B., Guitton, A., 2006. Imaging condition for reverse time migration. In: SEG Technical Program Expanded Abstracts 2006, pp. 2594–2598. https://doi.org/10.1190/1.2370059.
Khaksar, Z., McMechan, G.A., 2020. Angle-and azimuth-domain common-image gathers by reverse time migration for 3D elastic isotropic media. Geophysics 85 (3), S151–S167. https://doi.org/10.1190/geo2018-0795.1.
Liu, F., Zhang, G., Morton, S.A., et al., 2011. An effective imaging condition for reverse-time migration using wavefield decomposition. Geophysics 76 (1), S29–S39. https://doi.org/10.1190/1.3533914.
Li, Z., Zhang, H., Liu, Q., et al., 2007. Numeric simulation of elastic wavefield separation by staggering grid high-order finite-difference algorithm. Oil Geophys. Prospect. 42 (5), 510–515. http://www.ogp-cn.com.cn/CN/Y2007/V42/I5/510 (in Chinese).
Ma, D., Zhu, G., 2003. P- and S-wave separated elastic wave equation numerical modeling. Oil Geophys. Prospect. 38 (5), 482–486. http://www.ogp-cn.com.cn/CN/Y2003/V38/I5/482 (in Chinese).
Martin, G., Wiley, R., Marfurt, K., 2006. Marmousi2: An elastic upgrade for Marmousi. The leading edge 25 (2), 156–166. https://doi.org/10.1190/1.2172306.
Nguyen, B.D., McMechan, G.A., 2015. Five ways to avoid storing source wavefield snapshots in 2D elastic prestack reverse-time migration. Geophysics 80 (1), S1–S18. https://doi.org/10.1190/geo2014-0014.1.
Rosales, D.A., Biondi, B., 2005. Converted-waves angle-domain common-image gathers. In: SEG Technical Program Expanded Abstracts 2005, pp. 959–962. https://doi.org/10.1190/1.2148320.
Rosales, D.A., Fomel, S., Biondi, B., et al., 2008. Wave-equation angle-domain common-image gathers for converted-waves. Geophysics 73 (1), S17–S26. https://doi.org/10.1190/1.2148320.
Sava, P., Fomel, S., 2003. Angle-domain common-image gathers by wavefield continuation methods. Geophysics 68 (3), 1065–1074. https://doi.org/10.1190/1.1581078.
Sava, P., Fomel, S., 2006. Time-shift imaging condition in seismic migration. Geophysics 71 (6), S209–S217. https://doi.org/10.1190/1.2338824.
Sheriff, R.E., Geldart, L.P., 1995. Exploration Seismology, second ed. Cambridge University Press. https://doi.org/10.1017/CBO9781139168359.
Sun, R., 1999. Separating P- and S-waves in a prestack 2-dimensional elastic seismogram. In: European Association of Geoscientists and Engineers Extended Abstracts 1999, pp. 6–23. https://doi.org/10.3997/2214-4609.201407744.
Sun, R., McMechan, G.A., 2001. Scalar reverse-time depth migration of prestack elastic seismic data. Geophysics 66 (5), 1519–1527. https://doi.org/10.1190/1.1487098.
Sun, R., McMechan, G.A., Chuang, H., 2011. Amplitude balancing in separating P and S-waves in 2D and 3D elastic seismic data. Geophysics 76 (3), S103–S113. https://doi.org/10.1190/1.3555529.
Tang, C., McMechan, G.A., 2018. Multidirectional-vector-based elastic reverse time migration and angle-domain common-image gathers with approximate wavefield decomposition of P- and S-waves. Geophysics 83 (1), S57–S79. https://doi.org/10.1190/geo2017-0119.1.
Vyas, M., Nichols, D., Mobley, E., 2011. Efficient RTM angle gathers using source directions. In: SEG Technical Program Expanded Abstracts 2011, pp. 959–962. https://doi.org/10.1190/1.3627840.
Wang, C., Cheng, J., Arntsen, B., 2016. Scalar and vector imaging based on wave mode decoupling for elastic reverse time migration in isotropic and transversely isotropic media. Geophysics 81 (5), S383–S398. https://doi.org/10.1190/geo2015-0704.1.
Wang, J., Kuehl, H., Sacchi, M.D., 2005. High-resolution wave-equation AVA imaging: Algorithm and tests with a data set from the Western Canadian sedimentary basin. Geophysics 70 (5), S91–S99. https://doi.org/10.1190/1.2076748.
Wang, W., McMechan, G.A., 2015. Vector-based elastic reverse time migration. Geophysics 80 (6), S245–S258. https://doi.org/10.1190/geo2014-0620.1.
Whitmore, N., Crawley, S., 2012. Applications of RTM inverse scattering imaging conditions. In: SEG Technical Program Expanded Abstracts 2012, pp. 1–6. https://doi.org/10.3997/2214-4609.20130477.
Xiao, X., Leaney, W.S., 2010. Local vertical seismic profiling (VSP) elastic reverse-time migration and migration resolution: salt-flank imaging with transmitted P-to-S waves. Geophysics 75 (2), S35–S49. https://doi.org/10.1190/1.3309460.
Xu, S., Zhang, Y., Tang, B., 2011. 3D angle gathers from reverse time migration. Geophysics 76 (2), S77–S92. https://doi.org/10.1190/1.3536527.
Yan, J., Sava, P., 2008. Isotropic angle-domain elastic reverse-time migration. Geophysics 73 (6), S229–S239. https://doi.org/10.1190/1.2981241.
Yan, J., Sava, P., 2010. Analysis of converted-wave extended images for migration velocity analysis. In: SEG Technical Program Expanded Abstracts 2010, pp. 1666–1671. https://doi.org/10.1190/1.3513161.
Yang, K., Dong, X., Zhang, J., 2021. Polarity-reversal correction for vector-based elastic reverse time migration. Geophysics 86 (1), S45–S58. https://doi.org/10.1190/geo2020-0033.1.
Yang, K., Wang, X., Zhang, J., 2022. Elastic reverse time migration angle gathers using a stabilized Poynting vector without zero points within the wave propagation ranges. Geophysics 87 (3), S137–S150. https://doi.org/10.1190/geo2021-0415.1.
Yoon, K., Marfurt, K.J., 2006. Reverse-time migration using the poynting vector. Explor. Geophys. 37 (1), 102–107. https://doi.org/10.1071/EG06102.
Yoon, K., Guo, M., Cai, J., et al., 2011. 3D RTM angle gathers from source wave propagation direction and dip of reflector. In: SEG Technical Program Expanded Abstracts 2011, p. 3136. https://doi.org/10.1190/1.3627847.
Zhang, Q., McMechan, G.A., 2011. Direct vector-field method to obtain angle-domain common-image gathers from isotropic acoustic and elastic reverse time migration. Geophysics 76 (5), WB135–WB149. https://doi.org/10.1190/geo2010-0314.1.
Zhang, S., Du, Q., Zhang, X., 2018. Vector-based second-order divergence imaging condition for elastic reverse time migration. In: SEG Technical Program Expanded Abstracts 2018, pp. 4443–4447. https://doi.org/10.1190/segam2018-2997396.1.
Zhang, S., Lu, S., 2022. Residual moveout in angle gathers for converted waves. Geophysics 87 (3), U81–U92. https://doi.org/10.1190/geo2021-0366.1.
Zhang, Y., Sun, J., 2009. Practical issues in reverse time migration: true amplitude gathers, noise removal and harmonic source encoding. First Break 27 (1), 53–59.
Zhao, Y., Liu, T., Jia, X., et al., 2020. Surface-offset gathers from elastic reverse time migration and velocity analysis. Geophysics 85 (1), S47–S64. https://doi.org/10.3997/1365-2397.2009002.
Zhou, X., Chang, X., Wang, Y., et al., 2019. Amplitude-preserving scalar PP and PS imaging condition for elastic reverse time migration based on a wavefield decoupling method. Geophysics 84 (3), S113–S125. https://doi.org/10.1190/geo2017-0840.1.
Zhang, J., Tian, Z., Wang, C., 2007. P- and S-wave separated elastic wave equation numerical modeling using 2D staggered-grid. In: SEG Technical Program Expanded Abstracts 2007, SEG-2007-2104. https://doi.org/10.1190/1.2792904.